JOURNAL OF THERMOPHYSICS AND HEAT TRANSFER
Vol. 19, No. 1, January–March 2005

Impact of Flowfield–Radiation Coupling on Aeroheating for Titan Aerocapture

Michael J. Wright,* Deepak Bose,† and Joe Olejniczak*
NASA Ames Research Center, Moffett Field, California 94035

A methodology is developed that enables fully coupled computation of three-dimensional flow fields including radiation, assuming an optically thin shock layer. The method can easily be incorporated into existing computational fluid dynamics codes and does not appreciably increase the cost or affect the robustness of the resulting simulations. Further improvements in the accuracy of radiative heating predictions in an optically thin gas can be achieved by using a view-factor method rather than the standard tangent slab approach. These techniques are applied to the Titan aerocapture aeroheating problem, which is dominated by strong radiative heating. For this application, neglecting the nonadiabatic effects caused by radiation coupling results in an overprediction of radiative heating levels by about a factor of 2. Radiative coupling effects also significantly lower predicted convective heating by reducing boundary-layer edge temperatures. In addition, it is shown that the tangent slab approximation overpredicts radiative heating levels by a minimum of 20% in the stagnation region for this application. Over an entire design trajectory, correctly modeling radiative heat transfer results in a more than a factor of 2 reduction in total stagnation-region heat load over an uncoupled analysis.

Nomenclature

A_1–A_5	=	curve fit constants in Eq. (5)
E	=	radiative emission, W/m^3 · sr
N	=	number density, particles/m^3
Q	=	heat load, J/cm^2
q	=	heat flux, W/cm^2
T	=	temperature, K
t	=	time, s
V	=	velocity, m/s
z	=	$10{,}000/T_{ve}$, 1/K
α_r	=	tangent slab correction factor
Γ	=	Goulard number [Eq. (3)]
ΔA	=	computational surface cell area, m^2
ΔV	=	computational cell volume, m^3
ε	=	emissivity
Θ	=	energy source term, W/m^3
κ	=	empirical constant defined in Eq. (4)
ν	=	radiation frequency, 1/s
ξ	=	geometric view factor, sr
ρ	=	density, kg/m^3
σ	=	Stefan–Boltzmann constant, 5.6691×10^{-8} W/(m^2 · K^4)

Subscripts

ad	=	adiabatic
coup	=	coupled
s	=	species number
ts	=	tangent slab
ve	=	vibroelectronic
w	=	wall
∞	=	freestream

Superscripts

C	=	convective
R	=	radiative

Introduction

THE NASA In-Space Propulsion Program is currently investigating aerocapture as a means of enabling or improving the cost-efficiency of several planetary missions. During an aerocapture maneuver, the actively controlled vehicle decelerates into the target orbit by dissipating energy aerodynamically during a single pass through the atmosphere. In this manner, the large mass of a propulsive deceleration system is replaced by the potentially much smaller mass of an aeroshell to protect the vehicle from aerodynamic heating during the maneuver. One candidate destination for which aerocapture looks attractive is Saturn's largest moon Titan. A recent systems analysis study[1] was performed to examine the benefits of aerocapture at Titan. The resulting baseline Titan aerocapture vehicle would be proposed as a follow-on to the joint NASA/ESA Cassini mission, which is scheduled to arrive at Saturn in 2004 and release the Huygens Titan entry probe.

As a part of the systems study,[1] a preliminary aerothermal analysis of the baseline Titan aerocapture vehicle was performed, assuming an entry velocity of 6.5 km/s (Refs. 2 and 3). These calculations showed that the predicted maximum stagnation point convective heating was moderate (40–45-W/cm^2 peak). However, this work also concluded that the heating due to shock-layer radiation will be much larger than the convective component.[3] The Titan atmosphere at aerocapture altitudes consists primarily of nitrogen, with small amounts of argon and methane. The atmospheric methane (up to 3% by volume) dissociates in the nonequilibrium shock layer, leading to the formation of cyanogen, or CN. The CN molecule is a strong radiator in both the violet [B–X] and red [A–X] bands and is responsible for more than 99% of the total predicted shock-layer radiation at low entry velocities (below about 8 km/s). Preliminary analyses[3] indicated that the radiative heating from CN at the stagnation point could be as high as 300 W/cm^2, or seven times as large as the convective component. These results were qualitatively consistent with previous analysis of the ballistic Huygens probe entry.[4–6] The previous systems analysis study also looked at the effects of chemical kinetics, entry state variations, and uncertainties in atmospheric composition on the computed convective and radiative heating levels.

The high radiative heat flux predicted during this analysis was the primary driver in determining thermal protection system (TPS)

Presented as Paper 2004-0484 at the AIAA 42nd Aerospace Sciences Meeting, Reno, NV, 5–8 January 2004; received 21 April 2004; revision received 12 July 2004; accepted for publication 13 July 2004.

*Senior Research Scientist, Reacting Flow Environments Branch, MS 230-2. Senior Member AIAA.

†Senior Research Scientist, ELORET Corp., MS 230-2. Member AIAA.

material selection and sizing.[7] However, the uncertainties in the predicted radiative heating levels were quite large, predominantly due to several simplifying assumptions that were made during the systems-level analysis. As a result of this study,[1–3] it was determined that reducing the uncertainties in the prediction of radiative aeroheating was of primary importance for the design of any future Titan entry mission. The prior analyses made three major assumptions:

1) The chemical-kinetic mechanism employed was sufficient to predict the amount of CN formed in the shock layer, and the electronic states of the resulting CN molecules were in a Boltzmann distribution at the mixture vibrational–electronic temperature.

2) The shock-layer radiation was not coupled to the fluid dynamics and chemical kinetics in the flowfield (i.e., the flow was adiabatic). Therefore, shock-layer radiation predictions could be performed as a postprocessing step after the computational fluid dynamics (CFD) was completed.

3) The distributed radiative heating on the vehicle could be adequately estimated via a tangent slab approximation with an appropriate scale factor to account for body curvature effects.

This paper presents a methodology for the computation of fully coupled convective and radiative heating for radiation in an optically thin gas, which will effectively eliminate the last two of these assumptions. This methodology is then applied to the Titan aerocapture problem. Results are shown only for the forebody of the Titan aerocapture vehicle, but the methodology can also be applied to the afterbody.[8] An assessment of the validity of the first assumption is still under investigation.

Titan Aerocapture Reference Concept

The baseline configuration from the systems analysis study is a 3.75-m-diam 70-deg sphere cone, shown in Fig. 1 (Ref. 1). The vehicle will fly at a constant angle of attack of 16 deg to achieve a lift-to-drag ratio of 0.25, which was found to be sufficient to enable robust guidance and control during the aerocapture maneuver. The ballistic coefficient was set at 90 kg/m^2. This vehicle would enter the atmosphere of Titan at a nominal relative velocity of 6.5 km/s, although alternate trajectories with entry velocities up to 10 km/s were also considered. Aeroheating analysis and mission design were conducted using a series of lift-up and lift-down design trajectories.[9] Trajectories were generated using three atmospheric density profiles,[10] which bounded the uncertainty in atmospheric density as a function of altitude. The atmosphere was assumed to consist primarily of nitrogen, with small amounts of methane and argon. The relative abundance of these trace species as a function of altitude was determined using an engineering-level atmospheric model (TitanGRAM),[10] which predicted methane mole fractions between 1 and 5% at aerocapture altitudes.

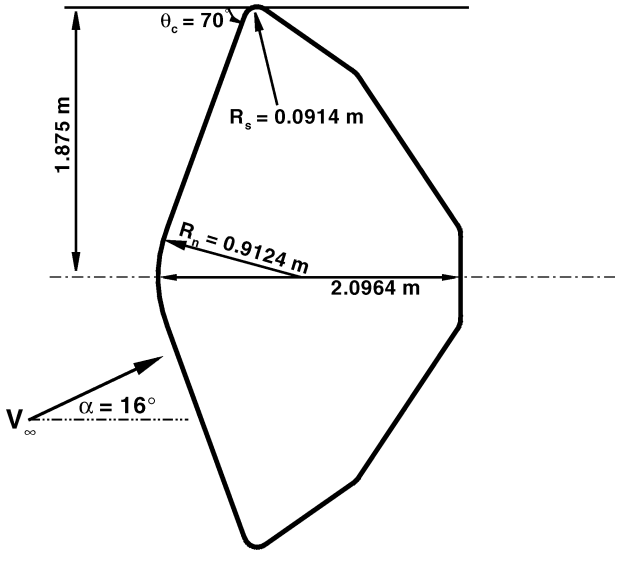

Fig. 1 Aeroshell configuration for the Titan aerocapture concept.

Physical and Numerical Models

The flowfield computations are performed using the CFD code DPLR.[11,12] DPLR is a parallel multiblock finite volume code that solves the reacting Navier–Stokes equations including finite-rate chemistry and the effects of thermal nonequilibrium. The Euler fluxes are computed using a modified (low-dissipation) form of Steger–Warming flux vector splitting,[13] with up to third-order spatial accuracy obtained via MUSCL extrapolation coupled with a minmod limiter.[14] Viscous fluxes are computed to second-order accuracy using a central difference approach. Time advancement to a steady-state solution is achieved using the data-parallel line relaxation method.[11] DPLR has been used previously for several other planetary-entry simulations.[2,12,15]

A detailed description of the relevant equations for atmospheric entry flows has been presented in a number of sources[16,17] and will not be repeated here. For typical Titan entry conditions thermal nonequilibrium effects will greatly influence the amount of predicted shock-layer radiation. Therefore, two energy equations are solved: a total energy equation and a vibroelectronic energy equation. In this formulation it is assumed that the vibrational and electronic modes of the gas are in equilibrium with each other, but not with the translational–rotational component.[17] This model was originally developed for air flows, but should be a reasonable approximation for the N_2-dominated Titan atmosphere (89–97% by mole) as well. The energy exchange between the translational–rotational and vibrational–electronic modes is modeled using a Landau–Teller formulation, where relaxation times are obtained from Millikan and White.[18] Characteristic vibrational temperatures for the simple harmonic oscillator approximation are taken from Gurvich et al.[19]

At the entry velocities considered, previous analysis[2] indicated that the flow is weakly ionized. However, this analysis also determined that the amount of ionization is small enough so that the effect on convective and radiative heating predictions is negligible. Therefore a 13-species (CH_4, CH_3, CH_2, N_2, C_2, H_2, CH, NH, CN, N, C, H, Ar) 15-reaction finite-rate chemistry model is used in this paper. However, for completeness one case was run using a 19-species, 22-reaction model, including the ions N_2+, CN+, N+, C+, and H+ as well as free electrons. In both cases the chemical source terms are modeled using rates collected for the Titan entry problem by Nelson et al.,[5] with the exception that the heavy-particle impact ionization reactions in Nelson et al. have been changed to electron impact ionization reactions as originally intended,[2] and the rates for those reactions have been updated to currently accepted values.[20] The complete reaction mechanism is given in Table 1. Following the work of Park,[21] the governing temperature for all dissociation reactions is assumed to be $T_a = \sqrt{(T\,T_{ve})}$. Equilibrium constants are computed using a minimized Gibbs free energy approach,[22] which eliminates the need to generate curve-fit expressions for each reaction. Species thermodynamic properties are modeled using the curve-fit expressions of Gordon and McBride.[22] A recent paper[23] examined the sensitivity of the predicted radiative heating to the reaction rates and other modeling parameters.

Viscosity and thermal conductivity are modeled using the species expressions and mixing rules presented by Gupta et al.[24] Collision integrals are taken from Park et al.[20] for most binary interactions. Collision integrals for all other interactions were computed using a modified Lennard–Jones potential[20] for the neutral–neutral interactions and a polarization potential for the ion–neutral interactions. The self-consistent effective binary diffusion method[25] is used to model diffusion fluxes. Either a laminar or a fully turbulent flow model is used, depending on the case. For turbulent flows, the compressible Baldwin–Lomax algebraic model[26] is implemented with a turbulent Schmidt number of 0.5 and a turbulent Prandtl number of 0.9. The surface is assumed to be fully catalytic (diffusion-limited) to all ions as well as N_2 and H_2 recombination, and noncatalytic to all other species. More rigorous surface boundary conditions could be applied if necessary, but the chemical energy contained in the trace carbonaceous species produced by methane decomposition is small compared to the total flow enthalpy, so little error is introduced by neglecting possible surface reactions of these species. A radiative equilibrium boundary condition is applied, with a constant

Table 1 Reaction rates for the Titan kinetic mechanism[a]

Reaction	C, $m^3/kmol \cdot s$	η	θ_r, K
Dissociation reactions ($T_a = \sqrt{T T_v}$)			
$C_2 + M \Leftrightarrow C + C + M$	9.68E+19	−2.0	71,000
$N_2 + M \Leftrightarrow N + N + M$	3.70E+18	−1.6	113,200
$CH + M \Leftrightarrow C + H + M$	1.13E+16	−1.0	40,913
$CN + M \Leftrightarrow C + N + M$	1.00E+20	−2.0	90,000
$CH_4 + M \Leftrightarrow CH_3 + H + M$	2.25E+24	−1.87	52,900
$CH_3 + M \Leftrightarrow CH_2 + H + M$	2.25E+24	−1.87	54,470
$CH_2 + M \Leftrightarrow CH + H + M$	2.25E+24	−1.87	50,590
$NH + M \Leftrightarrow N + H + M$	1.13E+16	−1.0	41,820
$H_2 + M \Leftrightarrow H + H + M$	1.47E+16	−1.23	51,950
Exchange reactions ($T_a = T$)			
$C + N_2 \Leftrightarrow CN + N + M$	1.11E+11	−0.11	23,000
$CN + C \Leftrightarrow C_2 + N + M$	3.00E+11	0.0	18,120
$C_2 + N_2 \Leftrightarrow CN + CN$	7.10E+10	0.0	5,330
$H + N_2 \Leftrightarrow NH + N$	2.20E+11	0.0	71,370
$H_2 + C \Leftrightarrow CH + H$	1.80E+11	0.0	11,490
$CN^+ + N \Leftrightarrow CN + N^+$	9.80E+09	0.0	40,700
$C + N \Leftrightarrow CN^+ + e$	1.00E+12	1.50	164,440
$C^+ + N_2 \Leftrightarrow N_2^+ + C$	1.11E+11	−0.11	50,000
$N + N \Leftrightarrow N2^+ + e$	1.79E+06	0.77	67,500
Electron impact ionization Reactions ($T_a = T_v$)			
$N + e \Leftrightarrow N^+ + e + e$	2.50E+31	−3.82	168,200
$C + e \Leftrightarrow C^+ + e + e$	3.70E+28	−3.00	130,720
$H + e \Leftrightarrow H^+ + e + e$	2.20E+27	−2.80	157,800

[a]Rate $= C T_a^{\eta} \exp(-\theta_r / T_a)$; M is a generic collision partner.

surface emissivity of 0.85, which is a representative value for the type of carbonaceous ablator typically used for such applications.[27]

The baseline computational grid for these simulations is a two-block nondegenerate topology, with a total of 132,000 grid points distributed around the 70-deg sphere-cone geometry. Sixty-five points were used in the body-normal direction, and 2028 total points were used in the two tangential directions. The grid for each computation was adapted using the self-adaptive grid code (SAGe)[28] to ensure that the outer boundary of the grid was aligned with the bow shock. Wall spacing was chosen to ensure that the cell Reynolds number at the wall was less than 5. This grid topology and density were shown previously[2] to provide grid-converged convective heating predictions for Titan aerocapture simulations, and direct comparisons between DPLR and the NASA Langley CFD code LAURA showed good agreement at that time. A grid refinement study of the predicted radiative heating levels will be presented in this paper.

Shock-layer radiation is calculated using the radiation transport code NEQAIR,[29] which computes the emission, absorption, and transport of radiation line by line using a tangent slab approximation. Based on previous analysis, at the entry velocities considered in this paper essentially all of the radiation comes from the CN violet $[B–X]$ (about 90% of the total) and red $[A–X]$ (about 10%) bands. The radiating species are assumed to be in a Boltzmann distribution at the mixture vibroelectronic temperature of the gas, which was found to be a reasonable approximation in previous work.[2,30] Detailed radiation calculations[3] have shown that, for the cases considered here, the radiative emission from CN is not significantly absorbed (the shock layer is optically thin), due in part to the relatively low shock-layer pressures. Therefore essentially all of the radiation produced at each point in the flowfield is emitted isotropically to space over a solid angle of 4π sr.

When NEQAIR is used, the total amount of radiation reaching the surface is integrated along each line of sight from the shock to the surface using a tangent slab approximation. In the tangent slab approximation, it is assumed that the input line of sight represents an infinite slab of gas parallel to the surface at that point. However, in reality the shock layer is curved due to body curvature. Therefore, a correction factor must be applied to the tangent slab result to account for surface curvature effects. The net radiative heating of the body then becomes

$$q^R = \alpha_r q^R_{\text{ts}} \tag{1}$$

The value of the correction factor α_r depends on the surface geometry and shock-layer conditions. For the stagnation region in blunt-body air flows, values between 0.75 and 0.85 are typically used.[29,31] The appropriate value to use away from the stagnation point is not well understood. A value of $\alpha_r = 1.0$ is frequently applied to the entire vehicle in an attempt to ensure conservatism in the radiative heating prediction. The accuracy of this approximation will be discussed later in the paper. A more detailed description of the application of NEQAIR to Titan entry radiative heating can be found in the work of Olejniczak et al.[3]

For the case of an optically thin gas, it is possible to eliminate the tangent slab approximation completely and use a view-factor-based approach to compute the radiative heating at each body point without simplification. In this case the radiative heating to the body is computed at each surface cell by summing the contribution from all emitting computational cells i:

$$\Delta q_i^R = \int \frac{E_i(\nu)\Delta V_i}{\Delta A}\xi_i \, \mathrm{d}\nu, \qquad q^R = \sum_i \Delta q_i^R \tag{2}$$

where the geometric view factor ξ_i (defined in Ref. 32) determines the fraction of the energy deposited on the surface element. For an optically thin gas the integral over frequency space in Eq. (2) can be evaluated simply from known transition probabilities. This computation is repeated at each surface cell to determine the distribution of radiative heating. Details on the implementation of this method can be found in Ref. 32.

Radiation Coupling

For the uncoupled simulations, the flowfield is first computed with DPLR, and the resulting solution is postprocessed to extract lines of sight for the radiation analysis. Lines of sight are generated normal to every surface grid point on the vehicle forebody, which yields an estimate of distributed surface radiative heating with the same spatial resolution as for the convective heating estimates.

The amount of coupling between the shock-layer radiation and fluid can then be estimated by evaluating the radiative cooling parameter, or Goulard number,[33] Γ:

$$\Gamma = 2q^R_{\text{ad}} \Big/ \left(\tfrac{1}{2}\rho_\infty V_\infty^3\right) \tag{3}$$

The factor of 2 in the numerator of Eq. (3) accounts for the fact that emission is isotropic; as much radiation is directed away from the surface as is directed toward it, and thus the total radiation flux along the stagnation line is twice that intercepted by the body. The radiative cooling parameter is essentially the ratio of the radiation energy flux to the total energy flux, and for optically thin gases it is a direct measure of the amount of flow energy converted to radiation. When Γ becomes large ($\Gamma > 0.01$) the flowfield is considered to be coupled, because the amount of flow energy converted to radiation has a significant impact on the fluid dynamics and chemical kinetics of the flow. The flowfield in this case becomes nonadiabatic, because energy can leave the computational domain via radiation transport.

The radiative cooling parameter was evaluated for the reference Titan aerocapture mission profile, based on the uncoupled aeroheating predictions from Refs. 2 and 3. At the peak convective heating point on the minimum atmosphere lift-up reference trajectory, the velocity was 5760 m/s and the freestream density was 1.49×10^{-4} kg/m^3. The uncoupled radiation analysis predicted 290 W/cm^2 of radiative heating at the three-dimensional stagnation point. By inserting these numbers into Eq. (3), we see that the Goulard number for this flow is approximately 0.4, indicating that the flow is strongly coupled. By comparison, $\Gamma \approx 0.01$ for the Fire II flight experiment,[34] and $\Gamma \approx 0.1$ for the Galileo probe.[35,36] The comparatively large values of Γ predicted for Titan aerocapture are due to the fact that CN is a strong radiator, and the atmospheric composition of Titan is ideal for CN formation behind a relatively low-speed shock wave.

The effect of modeling radiative cooling is to reduce the predicted net amount of shock layer radiation. Tauber and Wakefield[37] have

developed an engineering relation between Γ and the reduction in predicted stagnation-point radiative heating:

$$q^R_{\text{coup}} \big/ q^R_{\text{ad}} = 1/(1+\kappa\Gamma^{0.7}) \tag{4}$$

where the empirical constant κ is gas-mixture specific. Although Eq. (4) was originally developed for the optically thick shock layer encountered during Jupiter entry ($\kappa = 3$) (Ref. 37), it has been shown to provide reasonable results for strongly coupled air radiation by setting $\kappa \approx 3.45$, and thus should provide a reasonable first estimate of the effect of radiation coupling for this problem. For $\Gamma \approx 0.4$, Eq. (4) predicts a reduction in net radiative heating of more than 60% over the uncoupled result.

Weakly coupled flows have been computed previously using a loosely coupled approach,[38,39] in which flowfield and radiation solutions are alternated until convergence is reached. However, this method becomes intractable for cases with strong coupling due to the number of iterations between the CFD and radiation solvers required to achieve convergence. In the general case, simulation of a fully coupled flowfield requires the simultaneous solution of the reacting Navier–Stokes and the radiative transport equations. The result is a set of integrodifferential equations in which emission at any point in the flowfield has an essentially instantaneous effect on all other points. In addition, resolution of frequency space and solid-angle (emission direction) space greatly increases the dimensionality and complexity of the problem. Solution of this coupled equation set has been demonstrated previously,[40–42] but the resulting algorithms are extremely complex and time-consuming, particularly in three spatial dimensions. However, because the shock layer produced during Titan aerocapture was found to be optically thin to CN radiation in previous analysis,[3] it is possible to greatly simplify the coupled problem for Titan entries. In the case of an optically thin gas (assuming that induced emission and scattering effects are small) the analysis reduces to a pointwise computation of emission per unit volume. All radiation produced is assumed either to impact the body surface or to leave the computational domain without interacting with the rest of the flow. Thus, radiation coupling in an optically thin gas acts as a volumetric sink term in the relevant energy conservation equations.

The emission rates for CN red and CN violet radiation can be readily computed from known spectroscopic constants and transition probabilities.[43] Assuming a Boltzmann distribution of the excited states, emission per unit volume is a function only of the number density of CN molecules available to radiate and the vibroelectronic temperature of the gas. Although in principle the emission rates could be computed directly within DPLR, it was decided to curve-fit these rates in order to improve the overall computational efficiency of the resulting algorithm. Therefore, analytical fits of the NEQAIR-computed optically thin emission for CN red and CN violet emission are generated. For convenience, a curve-fit form used by Park[44] for equilibrium constants is borrowed:

$$E_{js} = N_s \exp\left(A_{1,js}/z + A_{2,js} + A_{3,js}\,\ell n(z) + A_{4,js} z + A_{5,js} z^2\right) \tag{5}$$

where E_{js} is the total radiative emission for molecular electronic band j of species s. Values of the constants A_1–A_5 for CN red and CN violet emission were obtained via a least-squares fitting process and are given in Table 2. These expressions are accurate to within 2% over the temperature range of interest (500–20,000 K). The curve-fit expressions are summed over the number of radiating species and the number of molecular bands for each species to compute the total emission in each cell:

$$E = \sum_s \sum_j E_{js} \tag{6}$$

Table 2 Curve fit parameters for CN violet [*B–X*] and red [*A–X*] emission

CN	A_1	A_2	A_3	A_4	A_5
Violet	−0.24820	−28.088	1.2171	−4.2147	0.02354
Red	−0.51122	−33.016	0.1590	−1.4679	0.00661

The result is inserted into DPLR as a sink term in the total and vibroelectronic energy equations to simulate the nonadiabatic energy loss due to conversion of flow energy to radiation. Note that, because the radiative emission is isotropic, a multiplicative factor of 4π steradians is required to convert from W/(m^3 · sr) to W/m^3 so that the resulting source term has the correct units in a finite-volume scheme of energy per unit volume per unit time. The resulting source term in the total and vibrational–electronic energy equations is then

$$\Theta^R = -4\pi E \tag{7}$$

where the negative sign indicates a sink of energy. In this manner, tight coupling between the flowfield and the radiation can be modeled with almost no performance penalty. It is important to note that even if the radiation were non-Boltzmann this approach would still be possible, although the functional form of the expressions for E_{js} would be more complex.

In addition to the volumetric sink terms that account for the energy loss from the shock layer, the portion of the radiation that strikes the surface must be accounted for in the radiative equilibrium surface energy balance (SEB):

$$q^C + q^R = \varepsilon\sigma T_w^4 \tag{8}$$

Note that conduction into the surface is assumed to be zero in Eq. (8), which is a standard conservative assumption used during preliminary design CFD analysis. The effects of conduction into the solid, as well as possible pyrolysis gas injection and ablation, are typically accounted for during response modeling and sizing of the TPS material. Although it is possible that ablation products may absorb CN radiation in the boundary layer, it is unlikely that significant absorption will occur given the optical transparency of the CN radiation. Possible interactions between ablation product gases and the boundary layer or radiation field are beyond the scope of the current work.

To account for the effects of radiative heating in the SEB it is necessary to compute the integrated radiative heat flux at each surface point in the computational grid, which can become complicated in a multiple-block grid topology on a distributed-memory parallel machine. Because the surface temperature varies as the fourth root of the heat flux [Eq. (8)], it was expected that radiative surface heating would have only a small impact on the flowfield. Therefore, for the purposes of this paper it was decided to implement this effect in a loosely coupled manner. In this approach, a simulation is first performed in which the volumetric (nonadiabatic) effects of radiation coupling are accounted for in the manner discussed above, but the surface heating effects are neglected [all of the emitted radiation is assumed to leave the flowfield and q^R is set equal to zero in Eq. (8)]. Radiative surface heating is then computed at each surface grid point in the initial solution, using either the tangent slab or view factor approach. This pointwise radiative heating distribution is read into DPLR as a boundary condition for the solver and a new solution is generated that accounts for radiative heating in the SEB. This process is repeated until convergence is reached. The net result of including radiative heating in the surface energy balance will be to increase the radiative equilibrium wall temperature over that predicted with only convective heating included. This increase in surface temperature will tend to decrease the thermal gradient between the wall and the boundary layer edge and thus should reduce the net convective heating to the wall slightly further. The effects of including radiative heating in the SEB will be quantified in the Results section.

Once a solution has been computed in DPLR, the radiative heating at each body point is obtained via a postprocessing step using either a tangent slab approach or the view-factor method discussed earlier. It is important to note that in either case the volumetric emission of the gas is fixed; the difference between the methods is in how the transport of that radiation to the surface is computed. Therefore either method is applicable to both uncoupled and coupled flowfield solutions.

Results

Several Titan aerocapture trajectories were generated during the previous systems analysis study. However, much of the aerothermal analysis was performed on the minimum atmosphere lift-up trajectory, which was predicted to yield the highest radiative heat fluxes.[3] The term "minimum atmosphere" refers to the use of the lower bound prediction for density as a function of altitude, as defined by Justus and Duvall.[10] The atmospheric composition for this trajectory was 95% N_2 and 5% CH_4 by volume and was assumed to be constant at aerocapture altitudes.[2] Peak convective heating was predicted to occur at $t = 253$ s on this trajectory, which corresponds to an angle of attack of 16 deg, $\rho_\infty = 1.49 \times 10^{-4}$ kg/m^3, $V_\infty = 5.76$ km/s, and $T_\infty = 152.7$ K. This trajectory point will be the focus of the parametric analysis presented here. Maximum radiative heat loads were predicted to occur on the minimum atmosphere lift-down trajectory.[3]

Figure 2 shows the computed uncoupled laminar convective heating on the forebody of the Titan aerocapture vehicle at this trajectory point. The computation was performed with a 13-species gas model; that is, ionization was neglected. The effect of ionization on the results will be discussed below. The flow stagnation point is below the cone apex (at approximately $y = -0.8$ m) due to the 16-deg angle of attack. As shown in Fig. 2, peak convective heating is 41 W/cm^2 and occurs at the sphere-cone apex rather than the flow stagnation point, due to flow expansion and the resulting boundary layer thinning around the apex. Figure 3 shows the uncoupled radiative heating on

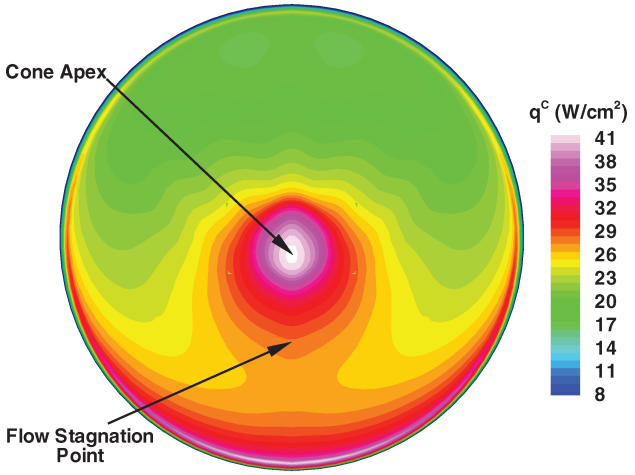

Fig. 2 Forebody convective heating assuming uncoupled radiation. Peak heating point ($t = 253$ s) on the minimum atmosphere lift-up trajectory.

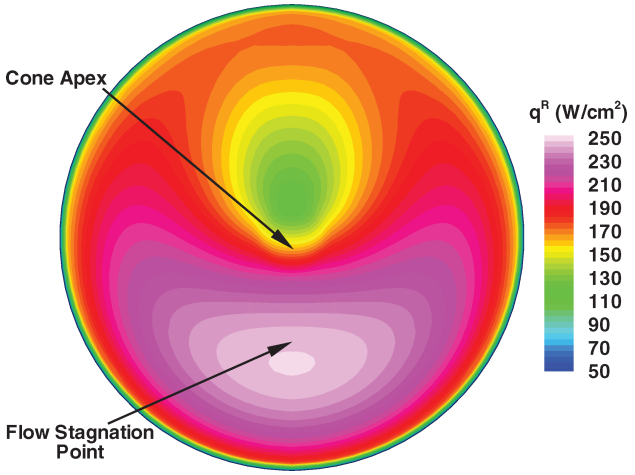

Fig. 3 Uncoupled forebody radiative heating computed using a view-factor method. Peak heating point ($t = 253$ s) on the minimum atmosphere lift-up trajectory.

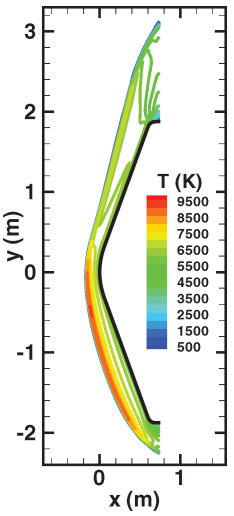

Fig. 4 Temperature contours in the symmetry plane. Peak heating point ($t = 253$ s) on the minimum atmosphere lift-up trajectory.

the forebody at this trajectory point computed using a view-factor method. Figure 4 shows the computed translational temperature in the symmetry plane for this case. From these figures we see that the peak radiative heating is 246 W/cm^2 and occurs near the flow stagnation point, because this is where the postshock temperatures are highest (larger emission per unit volume) and the shock standoff distances are largest (greater volume of radiating gas). This value is 24% lower than that previously reported using a tangent slab approximation (323 W/cm^2), indicating that the stagnation point correction factor $\alpha_r \approx 0.76$ for this case.[32]

Effects of Radiation Coupling

To evaluate the effects of radiation coupling on this flowfield, it is interesting to separate the volumetric (nonadiabatic) effects from the surface energy balance (SEB) effects, as discussed in the previous section. Therefore, we first simulate the same trajectory point, accounting for nonadiabatic flow coupling via Eq. (7), but neglecting the radiative heating in the SEB [$q^R = 0$ in Eq. (8)]. Figure 5a shows the impact of radiative coupling on the stagnation-line translational and vibro electronic temperature profiles. The radiative energy sink term has two main effects. First, removing energy from the flowfield causes the shock to move closer to the body, which decreases the total volume of radiating gas. For this case the shock standoff distance decreases from 29 to 24 cm. Second, by depleting energy from the vibroelectronic energy pool, the maximum postshock vibroelectronic temperature is decreased by about 850 K, from 8300 to 7450 K. This temperature decrease also reduces the amount of radiation emitted, because emission is a strong function of electronic temperature. Additionally, the depletion of vibroelectronic energy decreases the translational–rotational energy in the shock layer as well, due to the energy coupling terms between the translational and vibrational modes of the gas. Although the majority of the emission occurs in the hottest gas immediately behind the shock, the flow continues to lose energy to radiation as it convects down the stagnation streamline, and as a result the total temperature decrease between the shock and the boundary layer edge is greater for the coupled flow case. Figure 5a also shows that the maximum postshock translational temperature is essentially unaffected by coupling, because the peak translational temperature is reached immediately behind the shock wave before the vibroelectronic temperature has risen enough to generate excited CN molecules. At the boundary-layer edge the flow reaches thermal equilibrium in both solutions, but the edge temperature is about 2000 K lower for the coupled flow. This decrease in edge temperature reduces the thermal gradient through the boundary layer, which will decrease convective heating as well.

Figure 5b shows the computed volumetric emission along the stagnation streamline for the uncoupled and coupled simulations. In a tangent slab approximation, this emission would be directly integrated along the stagnation streamline to compute the stagnation-point radiative heat flux. From Fig. 5b we see immediately that the

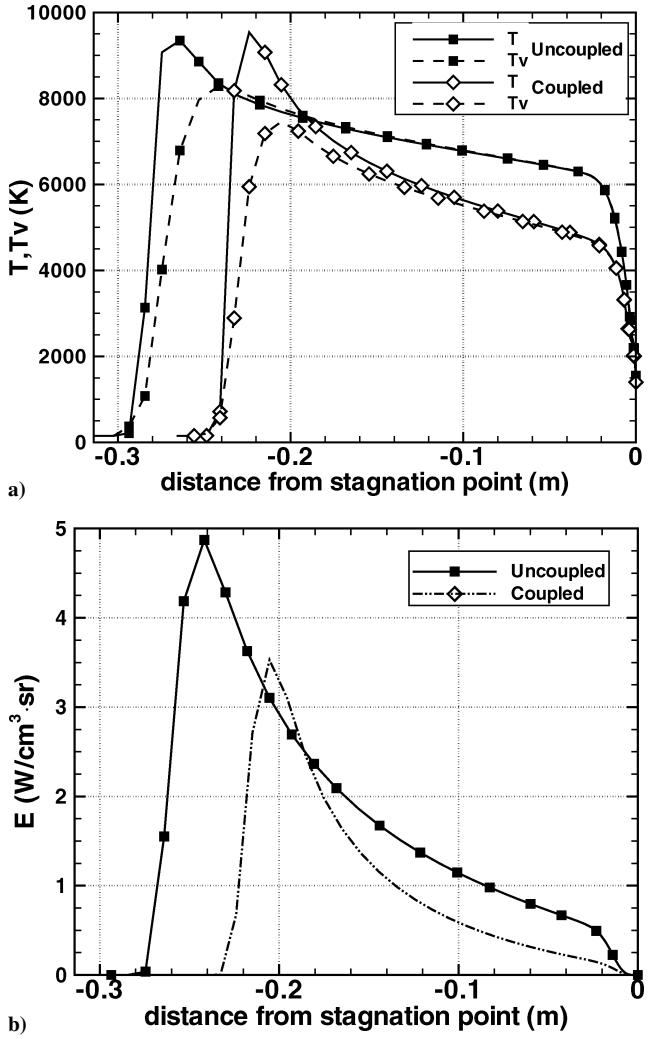

Fig. 5 Effect of coupling on stagnation-line a) temperatures and b) volumetric emission. Peak heating point ($t = 253$ s) on the minimum atmosphere lift-up trajectory.

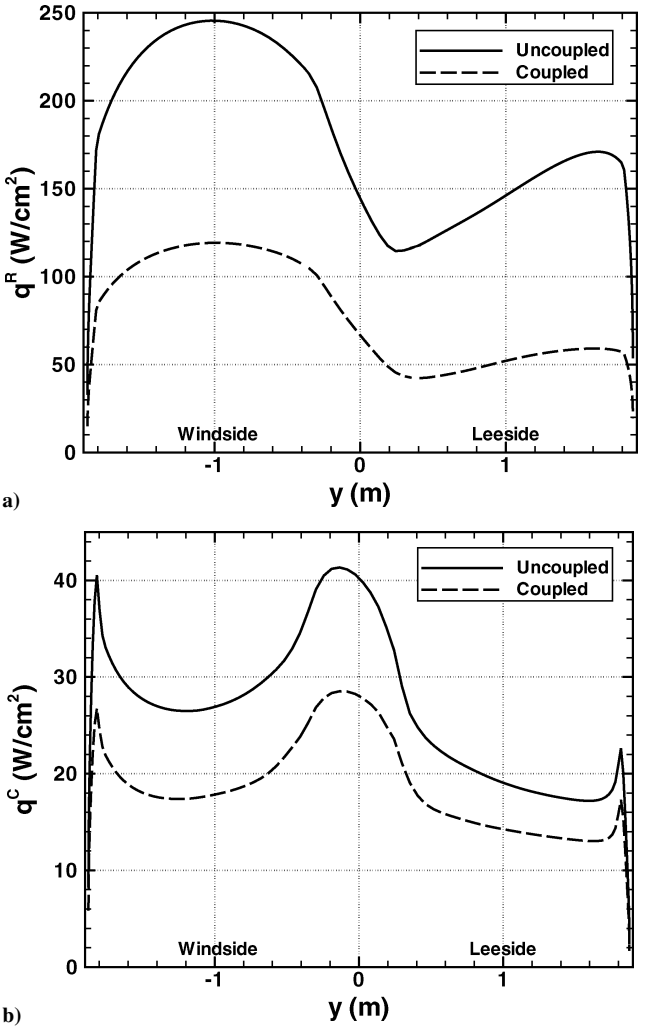

Fig. 6 Coupled vs uncoupled a) radiative and b) convective centerline heating. Peak heating point ($t = 253$ s) on the minimum atmosphere lift-up trajectory.

peak emission for both cases occurs at the location of peak vibrational, as opposed to translational, temperature. Although the peak emission occurs immediately behind the shock wave, in both cases Fig. 5b shows that there is significant emission from the entire volume of gas between the shock and the boundary-layer edge, and thus the typical tangent slab assumption of a thin layer of emitting gas is not valid for this flow. Finally, the figure also shows clearly that the coupled solution has less peak emission behind the shock wave (3.5 vs 4.9 W/cm$^3 \cdot$ sr), due to the decrease in peak vibrational temperature.

Figure 6a compares the coupled and uncoupled radiative heating along the centerline of the forebody of the Titan aerocapture vehicle for this case, computed with view factors. The stagnation point is at $y \sim -0.8$ m from the apex. The gaps in the lines are due to the multiblock topology; the radiative heating is computed at cell centers rather than vertices. Including the volumetric radiative coupling terms reduces the stagnation-region radiative heating by slightly more than a factor of 2, with a maximum of 119 W/cm^2 near the flow stagnation point as opposed to 246 W/cm^2 for the uncoupled case. By comparison, Eq. (4) with $\kappa = 3$ predicts a maximum radiative heating of about 101 W/cm^2. This result indicates that using Eq. (4) to estimate the impact of radiation coupling may be reasonable as long as an appropriate value of κ is selected. The same conclusion holds true if applied to the tangent slab predictions, where the uncoupled solution (Fig. 3) predicts a 323 W/cm^2 maximum and a coupled solution (not shown) predicts 156 W/cm^2, whereas Eq. (4) with $\kappa = 3$ predicts a net tangent slab radiative heating of 119 W/cm^2. From these results it is apparent that a universal value of κ in Eq. (4) does not exist for Titan CN radiation; selecting a value of $\kappa = 1.87$ would accurately reproduce the CFD results assuming tangent slab applies, but $\kappa = 2.25$ would be required for the view factor–based analysis.

The computed convective heating for the coupled calculation is compared with the uncoupled result in Fig. 6b. As expected, the convective heating is significantly reduced as a consequence of flow coupling, reaching a peak value of 28.5 W/cm^2 at the apex, as compared to 41 W/cm^2 for the uncoupled case. However, because laminar convective heating is still only a small portion of total predicted surface heating, the TPS design impact of this reduction would be small. Interestingly, the surface shear stress (not shown) is nearly the same for the coupled and uncoupled solutions. This result is not surprising, because the volumetric coupling terms directly reduce the internal energy of the gas, but have only an indirect effect on momentum.

The results in Fig. 6 were computed with full coupling in the volumetric sense, but with the impact of radiation on the SEB neglected. To assess the impact of including radiative heating in the SEB, the case was simulated using the loosely coupled methodology discussed previously. Figure 7a shows the computed translational and vibroelectronic temperatures along the stagnation line for these simulations. We see from Fig. 7a that including radiative heating in the SEB increases the radiative equilibrium wall temperature by about 700 K, but the shock layer is essentially unaffected. Because including radiation in the SEB does not alter shock-layer temperatures, it has no impact on volumetric emission or computed

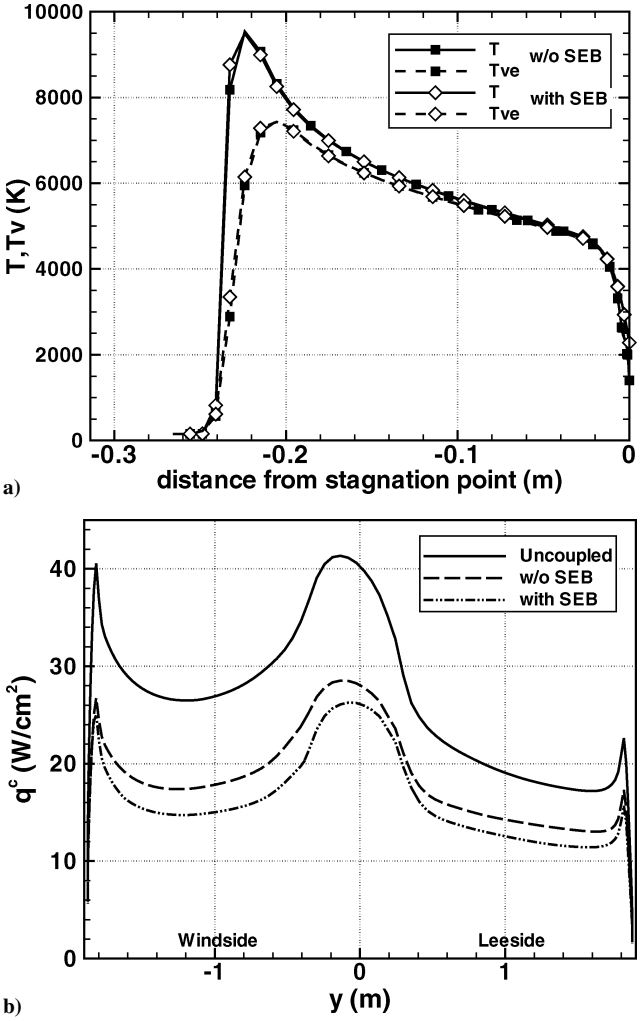

Fig. 7 Impact of including radiative heating in the SEB: a) stagnation-line temperatures and b) centerline convective heating. Peak heating point ($t = 253$ s) on the minimum atmosphere lift-up trajectory.

radiative heating. Therefore, only a single loosely coupled iteration is required to achieve a final solution. Figure 7b shows the impact of the SEB on the computed convective heating. Three lines are shown in Fig. 7b: an uncoupled solution, a solution with volumetric coupling only, and a fully coupled solution including surface-energy effects. Because the computed convective heating rate is not very sensitive to changes in wall temperature, including radiative heating in the SEB has a small impact on the computed convective heating. At the apex, the convective heating rate is reduced by 31% by the volumetric effects of radiation coupling, and only an additional 6% by the SEB terms.

Including radiation in the SEB significantly increases the cost of a simulation. Even if only a single loosely coupled iteration is required, the computer time is still approximately doubled, because two computations are required to arrive at the final result. Developing a completely coupled method would be even more expensive, because the relatively expensive view factor computation would then need to be performed each iteration or the geometrical factors would need to be stored as an additional array of dimension equal to number of surface points times number of volume cells. In addition, the energy balance presented in Eq. (8) also neglects conduction into the material, which is typically taken into account (together with convective and radiative heating) by a material-response model uncoupled from (or loosely coupled to) the CFD. Because, as shown in Fig. 7, including radiative heating in the SEB has no impact on computed radiation and only a small impact on computed convective heating, the remaining results shown in this paper will neglect this effect.

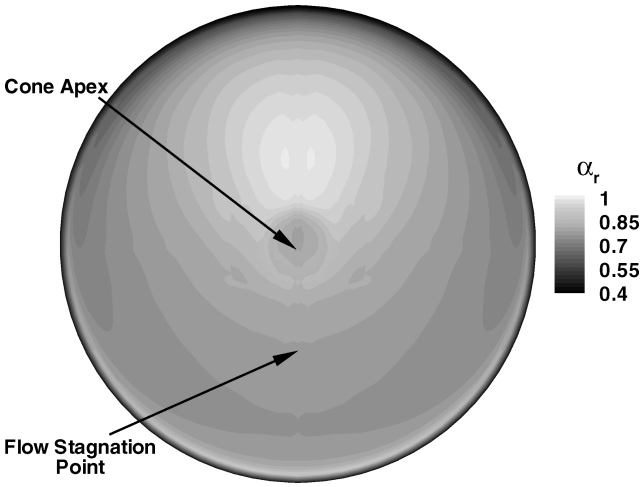

Fig. 8 Computed forebody tangent slab correction factor α_r. Peak heating point ($t = 253$ s) on the minimum atmosphere lift-up trajectory.

View Factor–Based Analysis

As stated previously, the tangent slab assumption will tend to overpredict radiative heating near the stagnation point, but it is not obvious a priori what the impact will be on other areas of the surface. To quantify the impact of using the tangent slab approach, Fig. 8 shows the computed value of α_r on the entire forebody for this case. From the figure we see that α_r is nearly constant at a value of about 0.76 on the entire wind side, which is not surprising because the vehicle is blunt and tangential gradients are small. On the lee side, α_r is larger (reaching a maximum value of about 0.92), because the shock standoff distance is smaller on the lee side and the shock itself is more planar (see Fig. 4), which better approximates the tangent slab assumption. The area where the tangent slab assumption is least accurate is the lee-side shoulder, where the flow is expanding rapidly and the tangent slab assumption fails to account for the small radius of curvature of the surface. These results are very similar to those presented previously for the uncoupled flow in Ref. 32.

The fact that α_r is always less than 1.0 in Fig. 8 means that the total amount of radiative energy reaching the surface is significantly less when view factors are used. The reasons for this result are clear if we think about the amount of radiation that reaches the surface from a given volume element. In the tangent slab approximation, it is assumed that exactly one-half of the isotropically emitted radiation eventually reaches the surface. However, in the view-factor approach, the actual subtended solid angle of the surface is computed for each volume element. Because of the fairly large shock standoff distance on the wind side, the strongest emitting volumes "see" a solid angle subtended by the surface that is about 30% smaller than the 2π sr assumed by tangent slab. Emitting volumes closer to the body direct more of their energy to the surface, until at very close distances the tangent slab approximation becomes nearly exact. The difference between the actual solid angle subtended by the surface and the 2π steradian maximum, when integrated over all emitting volumes, accounts for the reduction in total energy reaching the surface. Finally, it should be noted that at the very top of the shoulder the results presented here are not accurate, because the computational solution space ends at a plane perpendicular to the maximum radius point on the aeroshell, and any radiation emitted beyond this point is not included in the view-factor summation. However, this local effect should be fairly small because of the rapidly expanding and cooling gas in this region.

Grid Resolution

Although previous analysis[2] has shown that the baseline grid topology and density are sufficient to provide grid converged results for convective heating, it is also necessary to evaluate the grid density required for grid-independent radiative heating predictions. Radiative heating is due to emission from the hot shock layer, and thus it is expected that shock-layer resolution will be more important

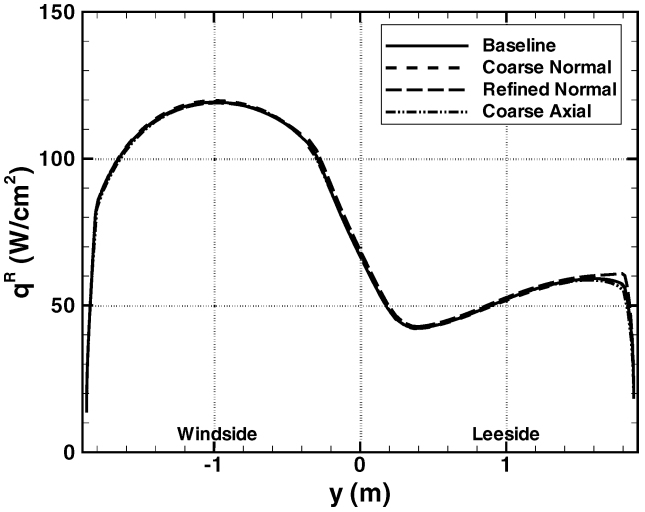

Fig. 9 Grid resolution study of computed centerline radiative heating. Peak heating point ($t = 253$ s) on the minimum atmosphere lift-up trajectory.

than boundary-layer resolution for this case. In particular, it is important to resolve gradients in T_{ve}, which govern the excited-state population of CN. From Fig. 5a it is apparent that gradients of T_{ve} are not large in the shock layer, and thus grid resolution requirements should not be too severe. Figure 9 shows the results of a grid resolution study performed at the peak heating point. The baseline grid has 65 body-normal points and 2028 tangential points distributed across the forebody, for a total of 132,000 points in the volume. The "coarse normal" grid has the same tangential distribution, but 25% fewer points in the body-normal direction (49 points). The "refined normal" grid has 50% more points in the body-normal direction (97 points). The "coarse tangential" grid has about half as many points in the tangential directions (1131 points), and the same normal distribution as the baseline. From Fig. 9 we see that the computed radiative heating along the vehicle centerline is essentially the same for all of these grids, In the stagnation region the predicted heating was about 1% higher than baseline for the "coarse normal" grid, and essentially identical to the baseline for the "refined normal" and "coarse tangential" grids. The largest differences occurred on the lee-side shoulder, but even in that region all solutions were within 3% of baseline. These results indicate that the baseline grid is indeed sufficiently resolved in both the tangential and normal directions.

Effects of Flow Ionization

A simulation was also performed to investigate the effect of ionization on the results presented here. For the uncoupled flow, the maximum mole fraction of electrons was found to be only about 3×10^{-4}. At this low level of ionization, there was essentially no change in the convective heating of the body (about 0.3 W/cm^2 difference at the apex, or 0.75%) or the radiative heating (about 2 W/cm^2 difference at the maximum heating point, or 0.75%) between the 13-species (nonionized) and 19-species flow simulations. The maximum electron mole fraction for the coupled flowfield was reduced more than an order of magnitude to $\sim 4 \times 10^{-5}$, due to the amount of energy lost to radiation. For this case there was no visible difference in either convective, radiative, or surface heating for the ionized vs nonionized flowfield. In general, radiation coupling will tend to suppress ionization. Therefore, if the effects of ionization are small for an uncoupled analysis, it can usually be safely neglected in the coupled analysis. However, ionization will become important at higher entry velocities.

Effects of Turbulence

Given the large size of the Titan aerocapture vehicle, engineering correlations predict that transition to turbulence will occur on the lee side of the forebody somewhere near the peak heating point of the trajectory.[2] The effects of turbulence on convective heating were

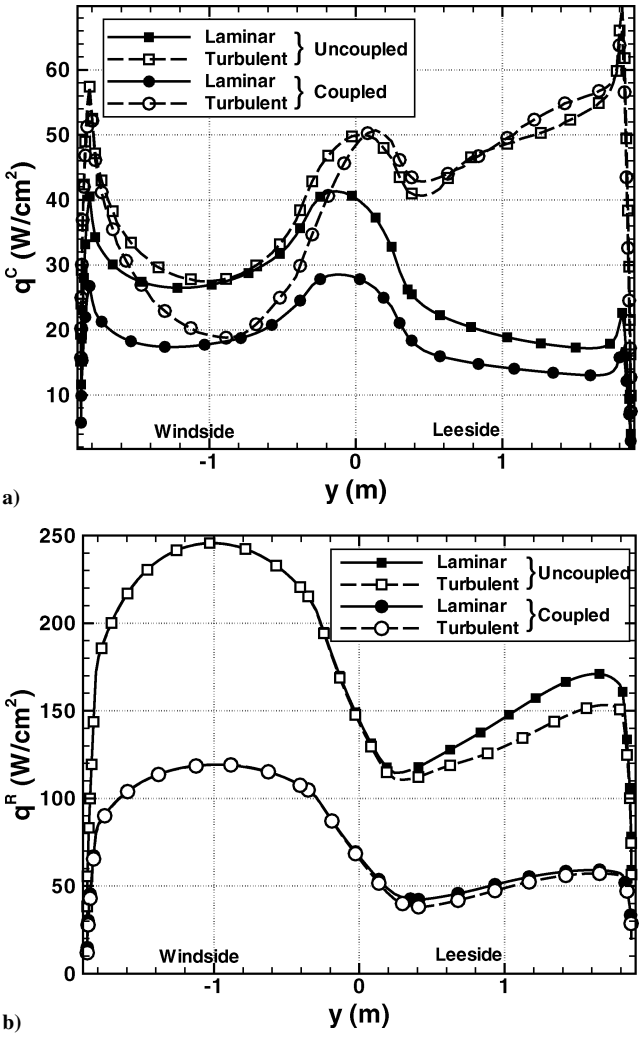

Fig. 10 Effect of turbulence: a) convective and b) radiative heating along the centerline of the Titan aerocapture vehicle. Peak heating point ($t = 253$ s) on the minimum atmosphere lift-up trajectory.

discussed in Ref. 2, but it is important to reexamine these results in the context of coupled radiation. Therefore, simulations of the $t = 253$ s point were also performed assuming that the flow was fully turbulent from the stagnation point, using a Baldwin–Lomax turbulence model. Before running a turbulent flow solution it is important to analyze the turbulence model to ensure its applicability to this problem. For example, the Baldwin–Lomax variant in DPLR by default relies on an enthalpy ratio search to locate the boundary-layer edge, which is typically assumed to lie at the point away from the wall where the total enthalpy reaches 99% of the freestream value. However, the coupled flowfield is nonadiabatic and thus total enthalpy is not conserved. Therefore, such a method will tend to locate the "boundary-layer edge" at the shock location, which is clearly not correct. For the coupled case shown here the boundary-layer edge was located by manually selecting a maximum body-normal index based on the boundary-layer location in the uncoupled solution. This approach is clearly not an effective solution to the problem, but it does permit comparisons to be made.

Figure 10a compares convective heating along the centerline for four computations including all combinations of laminar and turbulent flow and uncoupled and coupled radiation. The flow stagnation point is on the wind side at about $y = -0.8$ m from the apex. If we first look at the uncoupled results, we see that, as shown in Ref. 2, turbulent convective heating levels on the lee side of the forebody are as much as 2.5 times the laminar heating level, and even exceed the apex heating rate. There is also significant augmentation of windside heating levels away from the stagnation region ($y < -0.8$ m), although the laminar and turbulent results are nearly the same at

the stagnation point. When radiation coupling is included in the simulation, the laminar heating rate falls by 25–35% on the entire forebody, as discussed previously. Turning now to the coupled turbulent solution shown in Fig. 10a, a similar reduction in convective heating rate is observed in the stagnation area, but elsewhere the trend is quite different. In particular, on the lee side the turbulent convective heating is actually slightly higher for the coupled flow solution. However, the Baldwin–Lomax turbulent convective heating levels are sensitive to the computed boundary-layer edge location and can vary by up to 25% for this case depending on the chosen location. Therefore, because of the problems discussed in the previous paragraph, accurate simulations of the turbulent convective-heating levels for the coupled flowfield will likely require a more accurate turbulence model.

Radiative heating is primarily a function of shock-layer conditions and thus should not be affected by the modeling issues that have been discussed. Figure 10b compares radiative heating along the centerline for the same cases shown in Fig. 10a. For both the laminar and turbulent solutions the effect of coupling is to reduce radiative-heating levels by more than a factor of 2. Flow turbulence has essentially no effect on predicted radiative-heating levels on the wind side, which is not surprising because the effects of turbulence are confined to the boundary layer, where the gas is cool and not radiating. However, on the lee side the turbulent solutions show a small decrease (about 10%) in radiative heating. This decrease is likely due to the slight increase in shock standoff distance caused by the thicker turbulent boundary layer, but it was not explored in detail because the net effect is small.

Design Impact for Titan Aerocapture

The preceding analysis concentrated on the impact of radiation coupling at a single trajectory point where shock-layer radiation is significant. In order to understand the design impact of the improvements to CN radiation modeling presented here, the effect along an actual design trajectory must be evaluated. Therefore a series of cases are run at eight points along the minimum atmosphere undershoot trajectory, shown in Table 3. At each point a laminar uncoupled and a laminar coupled solution are computed so that the effects of radiation coupling can be quantified. Table 4 and Fig. 11 show the results for the point on the body in the stagnation region that experiences the maximum radiative heating. As can be seen from Fig. 11, radiation coupling has a significant impact on both convective and radiative heating levels throughout the trajectory. Computed heat loads for each case are shown in Table 5. For this trajectory, including radiation coupling in the simulation results in a 30% reduction in convective heat load and a 57% reduction in radiative heat load. The combined heat load is slightly more than a factor of 2 lower when radiation coupling is modeled, which highlights the importance of accurate modeling for this type of strongly coupled problem.

Table 3 Selected points on the minimum atmosphere lift-up trajectory

t, s	ρ_∞, kg/m^3	V_∞, m/s	T_∞, K	p_{stag}, Pa
174	4.697×10^{-6}	6558	131.9	190
198	1.697×10^{-5}	6512	143.2	680
228	6.414×10^{-5}	6273	150.9	2400
253	1.491×10^{-4}	5761	152.7	4700
266	2.051×10^{-4}	5371	152.7	5610
281	2.665×10^{-4}	4859	152.6	5960
312	3.338×10^{-4}	3862	152.3	4730
339	3.212×10^{-4}	3239	152.4	3320

Table 4 Stagnation region heating rates along the minimum atmosphere lift-up trajectory

	Uncoupled			Coupled		
t, s	q^C, W/cm^2	q^R, W/cm^2	α_r	q^C, W/cm^2	q^R, W/cm^2	α_r
174	8.4	24.4	0.81	6.2	4.0	0.78
198	14.1	78.7	0.78	8.9	21.5	0.78
228	23.8	166	0.77	15.1	72.8	0.78
253	28.2	246	0.76	18.7	119	0.76
266	27.1	270	0.76	18.0	121	0.77
281	23.6	213	0.77	16.1	86.6	0.76
312	11.8	13.6	0.79	10.5	10.5	0.77
339	5.5	0.2	——	5.5	0.0	——

Table 5 Stagnation region heat loads along the minimum atmosphere lift-up trajectory

Uncoupled		Coupled	
Q^C, J/cm^2	Q^R, J/cm^2	Q^C, J/cm^2	Q^R, J/cm^2
3,000	20,700	2,100	8,900

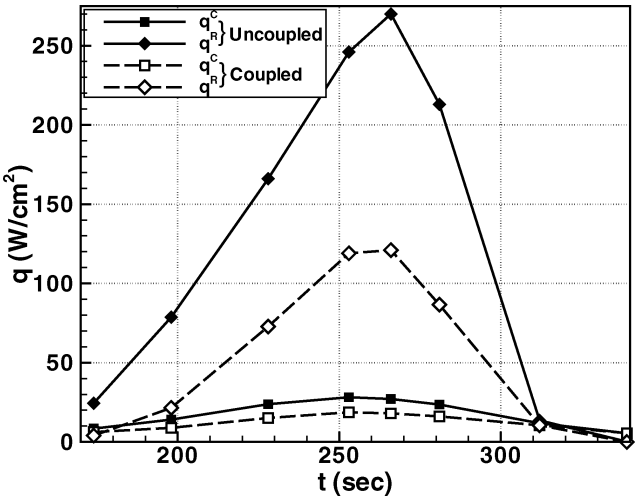

Fig. 11 Stagnation-point convective and radiative heating as a function of time on the minimum atmosphere lift-up design trajectory.

Finally, it is interesting to note that the tangent slab correction factor α_r at the stagnation point varies little with time, as shown in Table 4. In fact, to a good approximation a constant value of $\alpha_r = 0.77$ could be used in the stagnation region for all trajectory points, for both the uncoupled and coupled solutions. A similar comparison was performed at the apex of the sphere cone, and again a fairly constant value ($\alpha_r = 0.78$) was found to be sufficient for all trajectory points. This result is a little surprising at first, because the shock standoff distance varies considerably between the coupled and uncoupled solutions, and also varies with time during the entry. All else being equal, the value of α_r for a thin emitting shock layer is a strong function of the shock standoff distance.[32] Therefore, it seems logical to assume that, for example, the coupled solutions would have a larger value of α_r due to the decrease in shock standoff distance. However, this analogy is misleading for these flows, because significant emission is produced in the entire region between the shock wave and boundary-layer edge, which violates the assumption of a thin emitting layer. In fact, the shock layer appears to be roughly self-similar for these flowfields, which results in a nearly constant value of α_r at each point on the surface. Given the small variability in α_r with time, it is clear that a simple geometrically based constant value, based on the results of a single view-factor solution, would be a reasonable design assumption for this problem.

Conclusions

A new methodology is presented to enable the computation of fully coupled three-dimensional flowfields including the nonadiabatic effects of strong radiative emission in an optically thin shock layer. The method can easily be incorporated into existing CFD codes and does not appreciably increase either the cost or the

stability of the resulting simulations once the emission curve fits have been obtained. Using this method, the volumetric effects of radiation coupling were shown to be much more important than the impact of radiative heating on the surface-energy balance. In addition, the standard one-dimensional tangent slab method was replaced with a more accurate view factor–based approach for computing radiative heating.

These tools are applied to aeroheating simulations for a Titan aerocapture vehicle, which is an ideal demonstration case because Titan aeroheating is dominated by CN radiation produced in the optically thin shock layer. For this concept, previous uncoupled analysis predicted radiative heating rates of over 300 W/cm^2 at the stagnation point of the probe, as compared to convective heating rates of about 40 W/cm^2. By modeling the volumetric effects of radiation coupling on this flowfield, the net radiative-heating rates were shown to be more than a factor of 2 below the uncoupled estimates. In addition, use of the view-factor approach demonstrated that peak radiative heating in the stagnation region was about 25% less than that predicted using tangent slab at peak heating. The combination of these effects results in nearly a factor of 3 reduction in predicted maximum radiative heating levels for the Titan aerocapture vehicle. The energy lost from the flowfield through radiation also reduces convective heating to the body by as much as 30% near peak heating, because boundary-layer edge temperatures are considerably lowered. Comparison at multiple trajectory points demonstrated that the total heat load is reduced by a factor of 2 when coupling is properly modeled. Finally, it was shown that the ratio of radiative heating predicted by the view-factor and tangent slab methods is about $\alpha_r = 0.77$ in the stagnation region and does not vary significantly with time during the entry. Therefore, it appears feasible to use a tangent slab approach with an approximate "universal" correction factor to estimate stagnation-point radiative heating for a given vehicle geometry.

Although most other planetary entry problems of interest are not characterized by strong radiation and an optically thin shock layer, the methodology presented herein should prove useful for other simulations as well, because similar curve fits can be generated for any radiating species of interest. Many entry problems have a mix of important radiators, of which some are heavily absorbed, but others are optically thin. If the optically thin (or nearly optically thin) components of the shock-layer radiation are modeled in a coupled fashion, the resulting solution will be a better representation of the fully coupled result. At the least, such a solution will serve as a better starting point for a loosely coupled analysis, reducing the number of expensive iterations required for convergence.

Acknowledgments

This work was funded by the In-Space Propulsion program under task agreement M-ISP-03-18 to NASA Ames. The work performed by the second author was supported by prime contract NAS2-99092 to ELORET. The authors thank Dinesh Prabhu (ELORET) for his invaluable inputs into modeling techniques and aerothermal analysis of strongly radiating flowfields, Chul Park (ELORET) for clarification of the appropriate reaction rates for the electron impact ionization reactions, Michael Tauber (ELORET) for discussions on engineering relations for coupling effects on radiative heating in air, and Dinesh Prabhu and Ellis Whiting (ELORET) for their assistance in updating NEQAIR for Titan entry shock layer analysis.

References

[1]Lockwood, M., "Titan Aerocapture Systems Analysis," AIAA Paper 2003-4799, July 2003.

[2]Takashima, N., Hollis, B., Olejniczak, J., Wright, M., and Sutton, K., "Preliminary Aerothermodynamics of Titan Aerocapture Aeroshell," AIAA Paper 2003-4952, July 2003.

[3]Olejniczak, J., Prabhu, D., Wright, M., Takashima, N., Hollis, B., Sutton, K., and Zoby, V., "An Analysis of the Radiative Heating for Aerocapture at Titan," AIAA Paper 2003-4953, July 2003.

[4]Park, C. S., and Bershader, D., "Studies of Radiative Emission from the Simulated Shock Layer of the Huygens Probe," *Proceedings of the 18th International Symposium on Shock Waves*, Springer-Verlag, New York, 1992, pp. 671–676.

[5]Nelson, H. F., Park, C., and Whiting, E. E., "Titan Atmospheric Composition by Hypervelocity Shock Layer Analysis," *Journal of Thermophysics and Heat Transfer*, Vol. 5, No. 2, 1991, pp. 157–165.

[6]Baillion, M., Taquin, G., and Soler, J., "Huygens Radiative Probe Environment," *Proceedings of the 19th International Symposium on Shock Waves*, Springer-Verlag, New York, 1994, pp. 339–346.

[7]Laub, B., "Thermal Protection System Concepts and Issues for Aerocapture at Titan," AIAA Paper 2003-4954, July 2003.

[8]Olejniczak, J., Prabhu, D. K., Bose, D., and Wright, M. J., "Aeroheating Analysis for the Afterbody of a Titan Probe," AIAA Paper 2004-0486, Jan. 2004.

[9]Way, D., Powell, R., and Edquist, K., "Aerocapture Simulation and Performance for the Titan Explorer Mission," AIAA Paper 2003-4951, July 2003.

[10]Justus, C., and Duvall, A., "Engineering Level Model Atmospheres for Titan and Neptune," AIAA Paper 2003-4803, July 2003.

[11]Wright, M. J., Candler, G. V., and Bose, D., "Data-Parallel Line Relaxation Method for the Navier–Stokes Equations," *AIAA Journal*, Vol. 36, No. 9, 1998, pp. 1603–1609.

[12]Wright, M. J., Loomis, M. A., and Papadopoulos, P. E., "Aerothermal Analysis of the Project Fire II Afterbody Flow," *Journal of Thermophysics and Heat Transfer*, Vol. 17, No. 2, 2003, pp. 240–249.

[13]MacCormack, R. W., and Candler, G. V., "The Solution of the Navier–Stokes Equations Using Gauss-Seidel Line Relaxation," *Computers and Fluids*, Vol. 17, No. 1, 1989, pp. 135–150.

[14]Yee, H. C., "A Class of High-Resolution Explicit and Implicit Shock Capturing Methods," NASA TM 101088, Feb. 1989.

[15]Wercinski, P., Chen, Y.-K., Loomis, M., Tauber, M., McDaniel, R., Wright, M., Papadopoulos, P., Allen, G., and Yang, L., "Neptune Aerocapture Entry Vehicle Preliminary Design," AIAA Paper 2002-4812, Aug. 2002.

[16]Lee, J. H., "Basic Governing Equations for the Flight Regimes of Aeroassisted Orbital Transfer Vehicles," *Thermal Design of Aeroassisted Orbital Transfer Vehicles*, edited by H. F. Nelson, Vol. 96, Progress in Astronautics and Aeronautics, AIAA, New York, 1985, pp. 3–53.

[17]Gnoffo, P. A., Gupta, R. N., and Shinn, J. L., "Conservation Equations and Physical Models for Hypersonic Air Flows in Thermal and Chemical Nonequilibrium," NASA TP 2867, Feb. 1989.

[18]Millikan, R. C., and White, D. R., "Systematics of Vibrational Relaxation," *Journal of Chemical Physics*, Vol. 39, No. 12, 1963, pp. 3209–3213.

[19]Gurvich, L., Veyts, I., and Alcock, C. (eds.), *Thermodynamic Properties of Individual Substances*, 4th ed., Hemisphere, New York, 1991.

[20]Park, C., Jaffe, R., and Partridge, H., "Chemical-Kinetic Parameters of Hyperbolic Earth Entry," *Journal of Thermophysics and Heat Transfer*, Vol. 15, No. 1, 2001, pp. 76–90.

[21]Park, C., "Assessment of Two-Temperature Kinetic Model for Air," *Journal of Thermophysics and Heat Transfer*, Vol. 3, No. 3, 1989, pp. 233–244.

[22]Gordon, S., and McBride, B. J., "Computer Program for Calculation of Complex Chemical Equilibrium Compositions and Applications," NASA RP 1311, Oct. 1994.

[23]Bose, D., Wright, M., and Gökçen, T., "Uncertainty and Sensitivity Analysis of Thermochemical Modeling for Titan Atmospheric Entry," AIAA Paper 2004-2455, June 2004.

[24]Gupta, R. N., Yos, J. M., Thompson, R. A., and Lee, K., "A Review of Reaction Rates and Thermodynamic and Transport Properties for an 11-Species Air Model for Chemical and Thermal Nonequilibrium Calculations to 30,000 K," NASA RP 1232, Aug. 1990.

[25]Ramshaw, J. D., "Self-Consistent Effective Binary Diffusion in Multicomponent Gas Mixtures," *Journal of Non-Equilibrium Thermodynamics*, Vol. 15, No. 3, 1990, pp. 295–300.

[26]Brown, J., "Turbulence Model Validation for Hypersonic Flows," AIAA Paper 2002-3308, June 2002.

[27]Stewart, D. A., "Surface Catalysis and Characterization of Proposed Candidate TPS for Access to Space Vehicles," NASA TM 112206, July 1997.

[28]Davies, C. B., and Venkatapathy, E., "SAGE: The Self-Adaptive Grid Code, Version 3," NASA TM 208792, Aug. 1999.

[29]Whiting, E. E., Yen, L., Arnold, J. O., and Paterson, J. A., "NEQAIR96, Nonequilibrium and Equilibrium Radiative Transport and Spectra Program: User's Manual," NASA RP-1389, Dec. 1996.

[30]Labracherie, L., Billiotte, M., and Houas, L., "Shock Tube Analysis of Argon Influence in Titan Radiative Environment," *Journal of Thermophysics and Heat Transfer*, Vol. 10, No. 1, 1996, pp. 162–168.

[31]Park, C., "Stagnation Point Radiation for Apollo 4," AIAA Paper 2001-3070, June 2001.

[32]Bose, D., and Wright, M. J., "View-Factor Based Radiation Transport in a Hypersonic Shock Layer," *Journal of Thermophysics and Heat Transfer* (to be published).

[33]Goulard, R., "The Coupling of Radiation and Convection in Detached Shock Layers," *Journal of Quantitative Spectroscopy and Radiative Heat Transfer*, Vol. 1, 1961, pp. 249–257.

[34]Cauchon, D. L., "Radiative Heating Results from the Fire II Flight Experiment at Reentry Velocity of 11.4 km/s," NASA TM X-1402, July 1967.

[35]Tauber, M. E., Wercinski, P., Yang, L., and Chen, Y.-K., "A Fast Code for Jupiter Atmospheric Entry Analysis," NASA TM 1999-2208796, Sept. 1999.

[36]Moss, J. N., and Simmonds, A. L., "Galileo Probe Forebody Flowfield Predictions During Jupiter Entry," AIAA Paper 82-0874, Jan. 1982.

[37]Tauber, M., and Wakefield R., "Heating Environment and Protection During Jupiter Entry," *Journal of Spacecraft and Rockets*, Vol. 8, No. 3, 1971, pp. 630–636.

[38]Hartung, L., Mitcheltree, R. A., and Gnoffo, P. A., "Coupled Radiation Effects in Thermochemical Nonequilibrium Shock Capturing Flowfield Calculation," *Journal of Thermophysics and Heat Transfer*, Vol. 8, No. 2, 1994, pp. 244–250.

[39]Olynick, D. R., Henline, W. D., Hartung-Chambers, L., and Candler, G. V., "Comparison of Coupled Radiative Flow Solutions with Project Fire II Flight Data," *Journal of Thermophysics and Heat Transfer*, Vol. 9, No. 4, 1995, pp. 586–594.

[40]Gökçen, T., and Park, C., "The Coupling of Radiative Transfer to Quasi 1D Flows with Thermochemical Nonequilibrium," AIAA Paper 91-0570, Jan. 1991.

[41]Sakai, T., Tsuru, T., and Sawada, K., "Computation of Hypersonic Radiating Flowfield over a Blunt Body," *Journal of Thermophysics and Heat Transfer*, Vol. 15, No. 1, 2001, pp. 91–98.

[42]Matsuyama, S., Sakai, T., Sasoh, A., and Sawada, K., "Parallel Computation of Fully Coupled Hypersonic Radiating Flowfield Using Multiband Model," *Journal of Thermophysics and Heat Transfer*, Vol. 17, No. 1, 2003, pp. 21–28.

[43]Laux, C. O., "Optical Diagnostics and Radiative Emission of Air Plasmas," High Temperature Gasdynamic Lab., Rept. T-288, Stanford Univ., Stanford, CA, Aug. 1993.

[44]Park, C., *Nonequilibrium Hypersonic Aerothermodynamics*, Wiley, New York, 1990, p. 24.

Color reproductions courtesy of NASA Ames Research Center.